Journal of Metals, Materials and Minerals, 37(1), e2650, 2027

Synchrotron X-ray tomography and functional evaluations of lead-free piezoceramic-filled natural rubber composites

Chotiros DOKKHAN[1], Sirichai PATTANAWANIDCHAI[1], Chutima SAEHENG[1], Phakkhananan PAKAWANIT[2], Chumpon WICHITTANAKOM[3], and Jirapa TANGSRITRAKUL[4,*]

[1] *National Metal and Materials Technology Center, Thailand Science Park, Pathum Thani, 12120, Thailand*
[2] *Synchrotron Research and Applications Division, Synchrotron Light Research Institute, Nakhon Ratchasima, 30000, Thailand*
[3] *Department of Physics, Faculty of Science and Technology, Thammasat University, Pathum Thani, 12120, Thailand*
[4] *Department of Materials and Textile Technology, Faculty of Science and Technology, Thammasat University, Pathum Thani, 12120, Thailand*

***Corresponding author e-mail**: tjirapa@tu.ac.th

Received date:
11 February 2026
Revised date:
17 August 2026
Accepted date:
23 October 2026

Keywords:
Flexible electronics;
Lead-free piezoceramic;
BCZT;
Rubber composites;
Synchrotron X-ray tomography

Abstract

Flexible piezoelectric composite materials have gained increasing attention due to their widespread applications in modern electronic devices such as energy harvesters, dielectric capacitors, or wearable sensors. In this work, flexible piezoelectric composites were developed by incorporating BCZT lead-free piezoceramic fillers into a flexible NR matrix (NR/BCZT composites) with BCZT content ranging from 0 phr to 60 phr (referred as 0BCZT to 60BCZT). Additionally, the structure-property relationships of the NR/BCZT composites were evaluated using synchrotron X-ray tomographic microscopy (SR-XTM), in conjunction with various materials characterization techniques. This work found that the addition of BCZT filler into NR reduced cure time from 14.01 min (0BCZT) to 11.18 min (60BCZT), whereas hardness of the NR/BCZT composites increased from 40.18±0.08 to 45.92±0.11 with increasing BCZT content from 0 phr to 60 phr, respectively. Conversely, the tensile strength of the NR/BCZT composites at all compositions was lower than that of pure NR (tensile strength of 0BCZT = 24.70±2.56 MPa), except for the 30BCZT composite, which exhibited strong adhesion between the BCZT filler and the NR matrix and resulted in the observed highest tensile strength of 26.88±0.90 MPa. Interestingly, no increase in dielectric permittivity occurred at a low BCZT loading of 15 phr, while a significant enhancement from 2.76±0.13 to 3.34±0.08 was observed when the BCZT content was further increased from 15 phr to 30 phr, respectively. The filler dispersion in the NR matrix was investigated using synchrotron X-ray tomographic microscopy (SR-XTM), combined with quantitative analysis of SEM images. The results showed that, the interparticle spacing decreased with increasing the BCZT content in the NR/BCZT composites. This reduction in the interparticle spacing play an important role in the observed electrical properties of the NR/BCZT composites. These findings help to provide a better understanding of the development of lead-free piezoceramic-filled natural rubber composites.

1. Introduction

Piezoelectric materials are materials that can generate an electric charge when subjected to mechanical stress, known as the direct piezoelectric effect. Conversely, mechanical strain is generated when an electric field is applied, known as the converse piezoelectric effect [1,2]. Hence, various applications of piezoelectric materials have been developed. In recent years, flexible piezoelectric composite materials have gained increasing attention because they are widely found in modern electronic devices such as energy harvesters, dielectric capacitors, or wearable sensors [3–7]. Since the polarization observed in flexible piezoelectric polymers, such as the synthetic polymer poly(vinylidene fluoride) (PVDF) and its co-polymers, odd-numbered nylons, or and poly-L-lactic acid (PLLA), is still low compared to a well-known piezoelectric ceramic lead zirconate titanate (PZT), the incorporation of piezoelectric ceramics into flexible materials to form composites has been developed [2,6]. One of the most common types of flexible piezoelectric composites is the 0 to 3 type, which consists of zero-dimensional piezoceramic particles dispersed in a three-dimensional flexible material [7].

However, the toxicity of the hazardous lead (Pb) element in the well-known PZT piezoceramic poses risks to the environment and human health, leading to restrictions in many countries. As a result, lead-free piezoceramics have been developed by mimicking the so-called morphotropic phase boundary (MPB) features of PZT, which play a key role in the occurrence of excellent functional properties [1]. The $BaTiO_3$-based system $(Ba,Ca)(Zr,Ti)O_3$ (denoted as BCZT) is a promising lead-free piezoceramic candidate because it exhibits functional properties comparable to those of PZT while being more environmentally friendly [8]. Therefore, this work aims to enhance the functional properties of flexible piezoelectric composites by using BCZT lead-free piezoceramic as filler.

On the other hand, natural rubber (NR) has been extensively used as a flexible matrix in piezoelectric composites due to its renewable nature and remarkable flexibility [5,9–11]. For instance, Salaeh *et al.* investigated the addition of $BaTiO_3$ and $PbTiO_3$ fillers to unmodified NR and compared the results with those of epoxidized NR, which presented advantages such as high dielectric constant, lightweight, and good flexibility [9]. Conversely, González *et al.* found that the content of hydroxylate barium titanate ($BaTiO_3$-OH) filler in a vulcanized NR matrix played a crucial in the observed mechanical and electrical properties [10]. In addition, NR filled with $BaTiO_3$ filler whose surface was modified using a silane coupling agent (KH-570) showed a higher dielectric constant compared with NR composites containing unmodified $BaTiO_3$, as reported by El-Gamal *et al.* [11] Moreover, investigations of piezoelectric energy harvester based on NR filled with PZT have demonstrated promising voltage outputs, indicating that the flexible energy harvesters can be fabricated using NR filled with piezoceramic fillers [5]. However, to the best of our knowledge, no previous studies have reported the incorporation of BCZT piezoelectric fillers into an NR matrix.

Additionally, it is well known that the dispersion of fillers in a rubber matrix plays a significant role in the functional properties of the composites. Previous studies have employed synchrotron X-ray tomographic microscopy (SR-XTM) to investigate the role of fillers in the NR composites, as it is a non-destructive technique with a high-intensity synchrotron radiation that enhance X-ray image quality. [12–14] To date, no studies have employed SR-XTM to investigate the influence of BCZT filler dispersion in an NR matrix on its mechanical and electrical properties. Therefore, this work aims to develop piezoelectric composites by incorporating BCZT lead-free piezoceramic fillers into a flexible NR matrix and to study the structure-property relationships of the NR/BCZT composite using SR-XTM. Specifically, this study focuses on the effect of BCZT filler loading on filler dispersion within the NR matrix and the resulting mechanical and electrical properties of the NR/BCZT composites.

2. Experimental methods

$Ba_{0.85}Ca_{0.15}Ti_{0.9}Zr_{0.1}O_3$ lead-free piezoceramic filler (denoted as BCZT) used in this study was prepared via solid-state reaction technique using $BaCO_3$ (99.0%), TiO_2 (99.0%), $CaCO_3$ (99.0%), $BaZrO_3$ (99.0%) as precursors. All raw powders were weighed according to their stoichiometric proportions and mixed with ethanol (99.5%) at a powder-to-ethanol ratio of 1 g:1.2 mL in a polypropylene bottle using a ball mill with 5 mm Yttria Stabilized Zirconia (YSZ) beads for 24 h. The resulting mixture was then dried in an oven at 90°C overnight. Then, the mixed powders were calcined in an alumina crucible at 1250°C for 3 h with a heating rate of 5°C·min^{-1}. Next, 150 g of the calcined powders were remilled in ethanol at the same powder-to-ethanol ratio in a polypropylene bottle for another 24 h to obtain a fine BCZT powder. The remilling process was performed using a ball mill with YSZ beads of two different sizes, 2 mm and 5 mm in diameter, with 150 g of each bead size.

Table 1 shows the chemical composition used to prepare the BCZT piezoceramic-filled natural rubber composites (NR/BCZT composites) with BCZT content ranging from 0 phr to 60 phr (referred as 0BCZT to 60BCZT). In this work, the natural rubber was compounded with the vulcanizing agents using an internal mixer with a fill factor of 0.8 and a rotational speed of 50 rpm at 60°C for 10 min. First, natural rubber (NR) was masticated for 2 min. Subsequently, zinc oxide (ZnO), stearic acid, and butylated hydroxytoluene (BHT) were added to the masticated rubber and mixed for an additional 1 min. BCZT was then incorporated, and the mixture was further mixed for 5 min. Finally, the curatives, including N-tert-butyl-2-benzothiazolesulfenamide (TBBS), tetrabenzylthiuram disulfide (TBzTD), and sulfur, were added and mixed for a further 2 min. The resulting rubber compound was then discharged from the mixer. After that, a Moving Die Rheometer (MDR; TechPro MD+, USA) was employed to examine the curing characteristics of each composition in accordance with ISO 6502-3:2023. Next, 2 mm-thick sheets of NR/BCZT composites were prepared by hot compression at 150°C for the optimum cure time (t'c(90)) of each composition as determined by a MDR.

Table 1. Chemical composition for preparing the NR/BCZT composites with BCZT loading from 0 phr to 60 phr.

Materials	Loading [phr[1]]
Natural rubber (NR)	100
$Ba_{0.85}Ca_{0.15}Ti_{0.9}Zr_{0.1}O_3$ (BCZT)	0, 15, 30, 45, 60
Zinc oxide (ZnO)	5
Stearic acid	2
N-Tertiarybutyl-2-benzothiazole sulfenamide (TBBS)	0.75
Tetrabenzylthiuram disulphide (TBzTD)	0.25
Sulfur	2
Butylated hydroxytoluene (BHT)	1

[1] part per hundred rubber

For material characterization, an X-ray diffractometer (Bruker D2 Phaser, Germany) was employed to investigate phase formation of the BCZT filler, while the particle size was determined using a particle size analyzer (Malvern Instruments Hydro 2000S, UK). The morphology and elemental analysis of BCZT filler and NR/BCZT composites was observed by Field-emission scanning electron microscope (JEOL JSM7800F, Japan) and Energy-dispersive spectroscopy (EDS) (Oxford X-Max 20, UK), respectively. Attenuated Total Reflectance Fourier Transform Infrared (ATR-FTIR) spectroscopy (Bruker INVENIO R, Germany) was conducted over a wavenumber range of 400 cm^{-1} to 4000 cm^{-1} at a resolution of 4 cm^{-1} with 64 scans to identify the functional groups of the NR/BCZT composites. Peak area of FTIR spectra for the BCZT filler and the NR matrix was evaluated by numerical integration using the Trapezoidal Rule. Tensile properties of the NR/BCZT composites were examined in accordance with ISO 37 using a universal testing machine (NARIN, NRI-TS500-20B(Extra), Thailand), whereas hardness was measured in accordance with ISO 48-4:2018 using a Shore A durometer (MonTect Rubber Hardness Tester Series HT 3000, Germany). For the mechanical tests, five specimens were tested for each compound, and the results are reported as the mean ± standard deviation.

For the characterization of electrical properties, three NR/BCZT composite specimens with a size of 10 mm × 10 mm for each composition were coated with air-dried silver electrodes on both parallel surfaces prior to electrical testing. The frequency-dependent dielectric properties were investigated by LCR meter (Keysight E4980AL, USA) over a frequency range of 0.1 MHz to 1 MHz, while field-induced polarization was measured under an applied bipolar field of ±20 kV·cm^{-1} with 2 Hz

using the Precision Premier II ferroelectric tester (Radiant Technologies, inc., USA). In this work, the average values of dielectric permittivity and loss tangent are reported as a function of frequency, while representative field-induced polarization curves for each composition are presented along with the average maximum polarization values obtained from four bipolar-field cycles.

In addition, filler dispersion in the NR/BCZT composites was investigated using synchrotron X-ray tomographic microscopy (SR-XTM) at beamline BL1.2 XTM, Synchrotron Light Research Institute, Thailand, with a photon energy of 1.2 GeV generated by a wigger source. To reduce artifacts, polychromatic X-rays were attenuated to a mean energy of 11.5 keV approximately using a 350 µm thick aluminum foil. Prior to data collection, the NR/BCZT composites were cut into small bar-shaped specimens with approximate dimensions (width × length × thickness) of 2 mm × 5 mm × 2 mm before being fixed to the sample holder using paraffin wax. For the topography scan, the X-ray projections over a 180° rotation with 0.1° angular increments were collected using a lens-coupled microscope and a scientific sCMOS camera (2560 pixel × 2160 pixels 16 bit), providing a optical resolution of 1.5 µm. Data pre-processing, background normalization, and computed tomography reconstruction were conducted using Octopus Reconstruction software. Conversely, three-dimensional (3D) visualization of the NR/BCZT composites was carried out using Drishti software.

3. Results and discussion

3.1 Characterization of the BCZT filler

Figure 1 shows the XRD pattern of the synthesized BCZT filler calcined at 1250°C for 3 h. The phase formation of BCZT was confirmed, as the diffraction peaks matched well with the BCZT perovskite phase (PDF 01-082-2813). However, traces of the calcium titanate ($CaTiO_3$) secondary phase were also observed in the XRD profile. This may be attributed to the decomposition of the $CaCO_3$ precursor into CaO and CO_2 at temperature range of 600°C to 700°C, as reported in thermal decomposition studies of calcite [15]. Consequently, CaO reacted with the TiO_2 precursor, resulting in the formation of the $CaTiO_3$ phase observed in this study. Although a pure BCZT perovskite phase could be obtained when the calcination temperature was further increased to 1350°C, undesirable large powder agglomeration occurred due to sintering effects, as also reported for BCZT powders by Mureddu *et al.* [16] In addition, the dielectric permittivity of $CaTiO_3$ ceramic ($\varepsilon r < 1000$) is significantly lower than that of BCZT ceramic ($\varepsilon_r \sim 2000$) [17,18]. Hence, the presence of $CaTiO_3$ may reduce the overall dielectric permittivity of the NR/BCZT composite.

In addition, it is well known that the functional properties of rubber composites are strongly dependent on the particle size and shape of the fillers, as these characteristics can influence the dispersion of the fillers within matrix. In this work, the particle size and morphology of the synthesized BCZT powder after ball milling using 2 mm and 5 mm diameter YSZ beads are presented in Figure 2(a–b), respectively. It was observed in Figure 2(a) that the particle size distribution of the BCZT powder is unimodal with the average particle size of 1.38 µm. Additionally, the prepared BCZT powder exhibited a narrow particle size distribution with D10, D50, and D90 values of 0.62 µm, 1.08 µm, and 2.06 µm, respectively, indicating high particle-size uniformity. Correspondingly, fine particles with irregular shapes were observed in the BCZT powder, as seen in Figure 2(b). These results imply that the BCZT powder suggest favorable dispersion in the rubber matrix due to the small particle size and high surface area, which consequently resulting in strong interfacial forces between the BCZT filler and the rubber matrix [9].

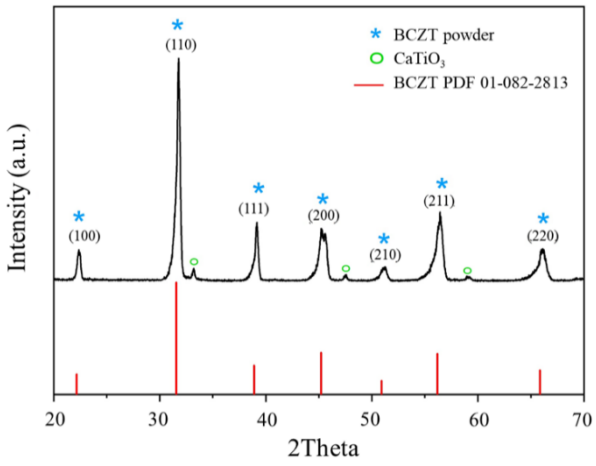


Figure 1. XRD pattern of the BCZT powder synthesized via solid-state reaction technique using calcination temperature of 1250°C for 3 h.

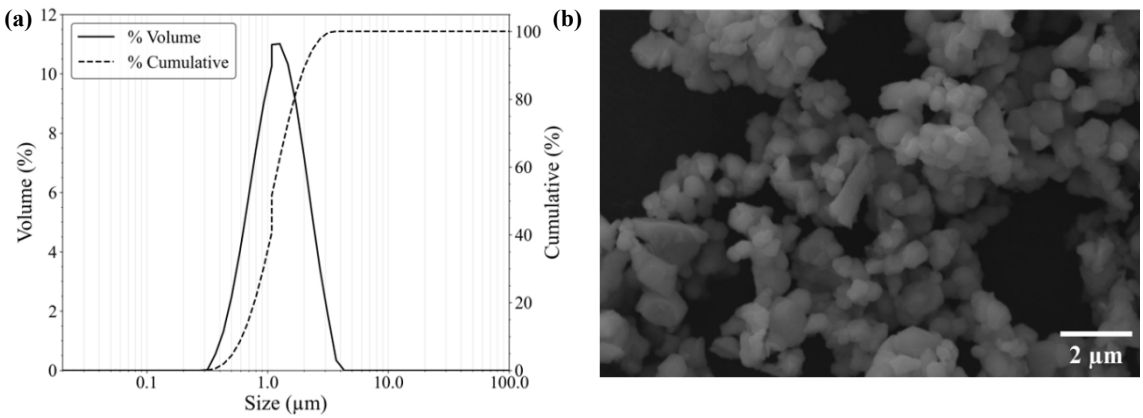


Figure 2. (a) Particle size distribution and cumulative percentage, and (b) morphology of the calcined BCZT powder after 24 h of milling using two sizes of YSZ beads.

3.2 Characterization of the NR/BCZT composites

The curing characteristics of the NR/BCZT composites with increasing BCZT loadings from 0 phr to 60 phr (denoted as 0BCZT to 60BCZT) are presented in Table 2. The minimum torque (M_L) and maximum torque (M_H) reflect the viscosity of the rubber compound and the extent of crosslinking in the cured rubber, respectively [11]. In this study, it was found that the delta torque (M_H–M_L) slightly increased with increasing BCZT content, indicating an enhancement of crosslinking during the vulcanization process within the NR/BCZT composites [19]. On the other hand, a progressive decrease in both scorch time (t_{s1}) and cure time ($t'_c(90)$) was observed with increasing BCZT loading, suggesting that the addition of BCZT filler enhances the vulcanization reaction rate [11].

Figure 3 illustrates the FTIR spectra of the NR/BCZT composites with varying BCZT content. The functional groups of the NR matrix in the NR/BCZT composites, as seen in Figure 3(a), were observed at wavenumber of 3045 cm^{-1} (=CH stretching), 2963 cm^{-1} (C–H stretching of CH_3), 2856 cm^{-1} (C–H stretching of CH_2 and CH_3), 1664 cm^{-1} (C=C stretching), 1449 cm^{-1} (C–H bending of CH_2), 1376 cm^{-1} (C–H bending of CH_3), and 837 cm^{-1} (C=CH wagging) [10]. In contrast, the Ti–O stretching mode of the BCZT filler in the NR/BCZT composites was observed at wavenumber between 570 cm^{-1} and 597 cm^{-1} [20]. Additionally, an enlarged view of the corresponding BCZT filler and the characteristic peak of the NR matrix is presented in Figure 3(b), with the BCZT filler observed at wavenumber between 570 cm^{-1} and 597 cm^{-1} and the NR matrix at ~837 cm^{-1}. It was found that the intensity of the corresponding BCZT peak increased with increasing BCZT content, while the intensity of the characteristic peak of the NR matrix remained stable. Moreover, quantitative analysis was conducted by calculating the peak area ratio (R) between peak areas of the BCZT filler and the NR matrix in the absorbance mode for each composition, as shown in Table S1 in the Supplementary document. The peak area ratio result demonstrated that the calculated R value gradually increased from 0 to 13.66 Abs·cm^{-1} with increasing BCZT loading from 0 phr to 60 phr. This finding indicates an increase in BCZT filler content within the NR/BCZT composites as the BCZT loading increased. Furthermore, no peak shift was observed for the characteristic NR peak at ~837 cm^{-1}, suggesting that no significant chemical interaction occurred between the NR matrix and the BCZT filler.

The morphology of the cross-sectional fracture surfaces of the NR/BCZT composites across all BCZT loadings (0 phr to 60 phr) is shown in Figure 4(a–e). Although no BCZT filler was added to the 0BCZT sample, the presence of particles was observed in this sample. Further elemental analysis of the 0BCZT sample using EDS detected Carbon (C = 87.75%), Oxygen (O = 5.05%), Zinc (Zn = 4.53%), and Sulphur (S = 2.67%), as shown in Figure S2 in the Supplementary document. This observation suggests that the particles observed in the 0BCZT sample are likely residues of zinc oxide (ZnO) vulcanizing agent dispersed in the NR matrix [21]. When adding BCZT filler into the natural rubber from 15 phr to 60 phr, the filler particles were dispersed separately within the NR matrix in all NR/BCZT composites, resulting in a 0 to 3 connectivity composite structure [9]. Moreover, no obvious agglomeration of the BCZT filler was observed in all NR/BCZT composites, suggesting that the relatively fine BCZT filler particles were suitable for dispersion within the NR matrix [6].

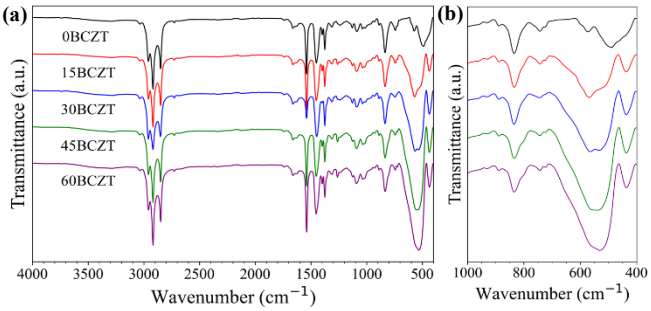


Figure 3. FTIR spectra of NR/BCZT composites with increasing the BCZT content in the wavenumber range of (a) 400 cm^{-1} to 4000 cm^{-1}, (b) the enlarged region between 400 cm^{-1} and 1000 cm^{-1}.

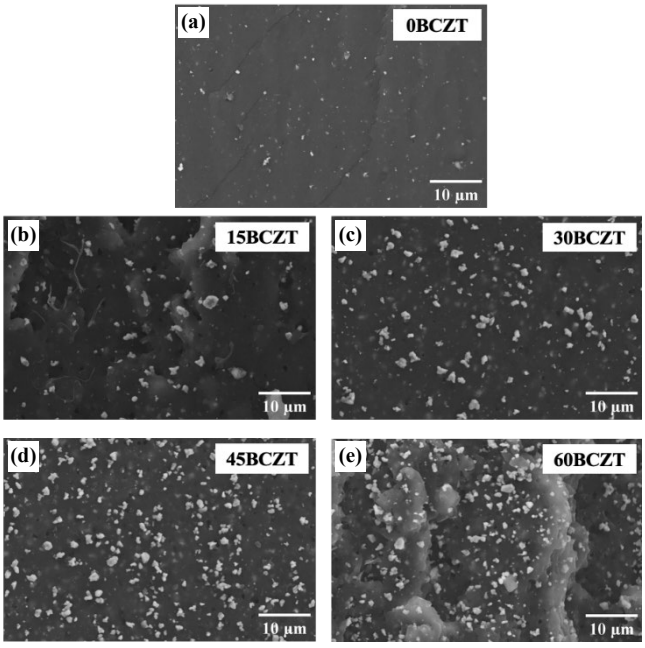


Figure 4. SEM micrographs of cross-sectional fracture surfaces of the NR/BCZT composites: (a) without BCZT loading, and (b–e) with BCZT loadings of 15 phr, 30 phr, 45 phr, and 60 phr, respectively.

Table 2. The curing characteristics at 150°C of natural rubber incorporating with BCZT filler from 0 phr to 60 phr.

Properties	0BCZT	15BCZT	30BCZT	45BCZT	60BCZT
Min. torque (M_L) (dN·m)	1.08	1.16	1.17	1.27	1.3
Max. torque (M_H) (dN·m)	7.36	7.68	8.15	8.83	9.24
Delta torque (M_H- M_L) (dN·m)	6.28	6.52	6.98	7.56	7.94
Scorch time (t_{s1}) (min)	9.88	9.7	8.75	8.76	8.71
Optimum cure time ($t'_c(90)$) (min)	14.04	13.4	12.05	11.87	11.18

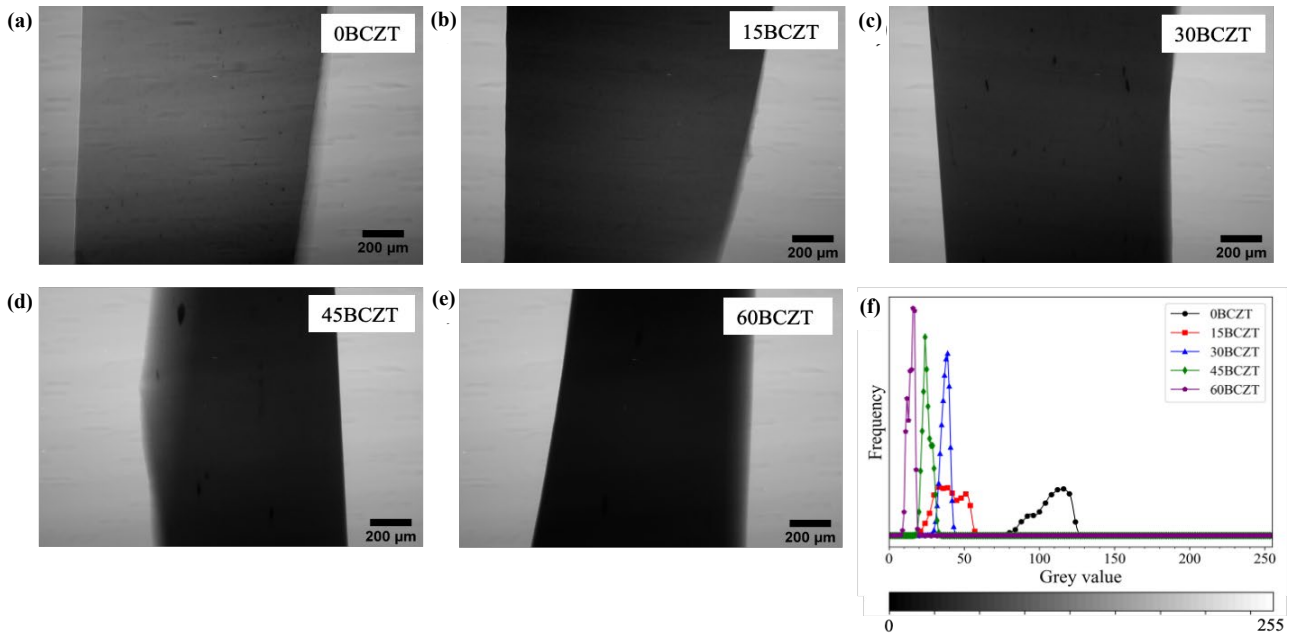


Figure 5. (a–e) 2D radiographic images of the NR/BCZT composites with BCZT loadings ranging from 0 phr to 60 phr, respectively, along with (f) comparison of their grayscale histogram.

3.3 Investigation of filler dispersion via SR-XTM study

Figure 5(a–e) presents the two-dimensional (2D) radiographic images of NR/BCZT composites obtained by synchrotron X-ray tomographic microscopy (SR-XMT), along with a comparison of the grayscale histograms of the NR/BCZT composite samples, as shown in Figure 5(f). Since the BCZT filler and NR matrix exhibit different linear attenuation coefficient (μ), filler dispersion was anticipated to be observable from the contrast in radiographic images of the 180° rotating NR/BCZT composites. However, the results revealed that as the BCZT content increased, the 2D radiographic images of the NR/BCZT composites appeared darker due to the increase density of BCZT filler in the NR/BCZT composite, resulting in enhanced X-ray attenuation [22,23]. Therefore, the intensity of transmitted X-rays through the NR/BCZT composites with the same thickness (~ 2 mm) dropped with increasing BCZT filler, leading to a gradual shift of the histogram peak corresponding to the NR/BCZT composites area toward lower values, as provided in Figure 5(f).

In addition, Figure 6 illustrates the internal three-dimensional (3D) visualizations of filler dispersion within NR/BCZT composites. It is worth noting that phase segmentation using Drishti software was employed to isolate regions of different densities within the 3D structure, corresponding to the NR matrix (~0.92 $g \cdot cm^{-3}$ [24]) and BCZT filler (~5.78 $g \cdot cm^{-3}$ [25]). However, in this work, phase segmentation between ZnO and BCZT particles within the NR/BCZT composites could not be achieved in the 3D visualization. Owing to their similar mass densities (~5.606 $g \cdot cm^{-3}$ for ZnO [26]), the resulting X-ray contrast was insufficient to distinguish the two particles. Therefore, the low-density or low-attenuation NR matrix and high-density or high-attenuation particles, including the BCZT filler and residual ZnO could be distinguished in the resulting 3D visualization. For 0BCZT composition, the particles observed in Figure 6(a) are attributed to ZnO residues from the vulcanizing agent in the NR matrix, as described earlier in SEM results shown in Figure 4(a) and the corresponding EDS spectrum presented in Figure S2 of the Supplementary document. With the addition of BCZT filler for 15 phr, the 3D visualization shows a greater number of fine particles homogenously distributed throughout the sample as observed in Figure 6(b). However, as the BCZT filler content increases from 30 phr to 60 phr, the presence of fine particles drastically decreases and disappears in the 60BCZT composites. Only large agglomerations of particles are shown in the 3D visualizations, as displayed in Figure 6(c–d). This may be attributed to the resolution limit of the optical system at the beamline [27]. Since the spatial resolution of the optical system used in this study was 1.5 µm, it could not resolve fine particles with interparticle distances below 1.5 µm.

To clarify this point, quantitative analysis of SEM images was further conducted to determine the two-dimensional nearest-neighbor distance (NND), which represents the center-to-center spacing between each particle and its nearest neighboring particle. Details of image-processing procedure and results are provided in the Supplementary document [28–30]. Figure 7 shows representative SEM micrographs and their corresponding ImageJ particle analyses of 30BCZT and 45BCZT composites for determining the NND. The quantitative analysis revealed that the mean NND decreased from 2.36 ± 1.00 µm for 30BCZT composite to 1.66 ± 0.69 µm for 45BCZT composite, corresponding to an approximately 30% reduction in the average nearest-neighbor spacing. The median NND similarly decreased from 2.09 µm to 1.52 µm. Thus, increasing the BCZT content primarily increased the population density of BCZT particle regions and reduced their interparticle spacing, approaching the resolution limit of the optical system at high BCZT loading. As a result, fine BCZT particles in the NR/BCZT composites with high BCZT loadings could not be resolved in the 3D visualizations shown in Figure 6(c–d). Note that the NND values were interpreted as apparent two-dimensional centroid-to-centroid distances derived from the SEM images, rather than as true three-dimensional surface-to-surface distances between BCZT particles.

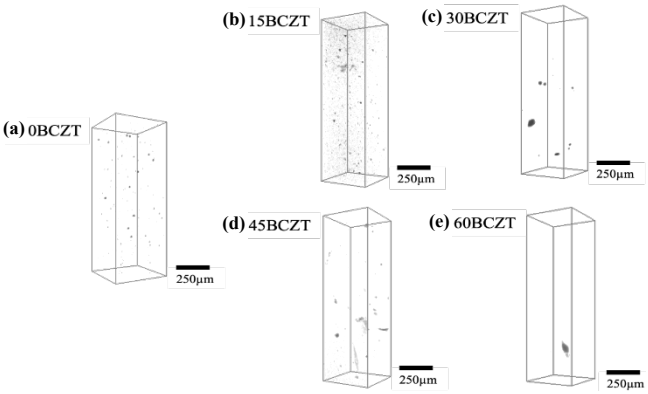


Figure 6. (a–e) 3D visualizations of filler dispersion in the NR matrix with increasing BCZT content from 0 phr to 60 phr, respectively.

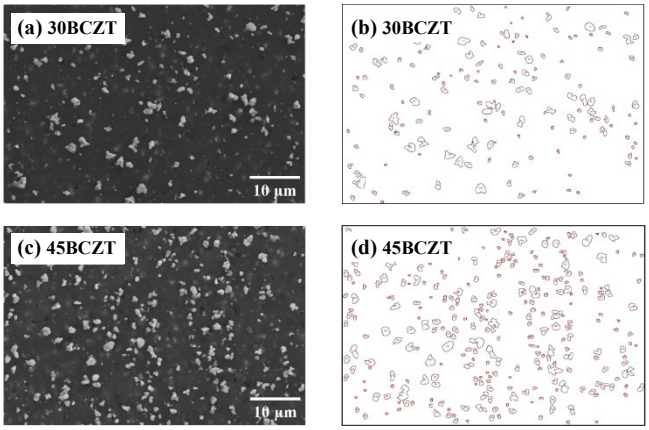


Figure 7. Representative SEM micrographs and corresponding ImageJ particle analyses of NR/BCZT composites: (a) original SEM micrograph of 30BCZT, (b) BCZT particles identified in 30BCZT, (c) original SEM micrograph of 45BCZT, and (d) BCZT particles identified in 45BCZT.

3.4 Mechanical properties of the NR/BCZT composites

The effects of BCZT filler addition into the NR matrix on the tensile properties and hardness are shown in Figure 8. The addition of BCZT into NR reduced the tensile strength of the NR/BCZT composites, except for the 30 phr composite which exhibited a slight increase in tensile strength from 24.70 ± 2.56 MPa at 0 phr to 26.88 ± 0.90 MPa at 30 phr, as seen in Figure 8(a). Moreover, one-way ANOVA was employed to determine the statistical significance of differences in tensile properties. The results showed a p-value of 0.030 for tensile strength, indicating a statistically significant difference ($p<0.05$). Furthermore, Figure 8(b) revealed that the incorporation of BCZT filler significantly increased the modulus at 300% strain from 2.98 ± 0.65 MPa (0 phr) to 4.01 ± 0.24 MPa (60 phr), with a p-value of 0.045. Conversely, the addition of BCZT filler to NR matrix from 0 phr to 60 phr did not significantly influence the elongation at break ($p = 0.832$), as shown in Figure 8(c). On the other hand, Figure 8(d) shows a gradual increase in hardness (shore A) from 40.18 ± 0.08 to 45.92 ± 0.11 with increasing BCZT filler loading from 0 phr to 60 phr, respectively. This result is attributed to the presence of BCZT filler in the NR matrix, which restricts the mobility of rubber chains and enhances the stiffness of the composites [11].

High magnification (10,000x) SEM analysis of the cross-sectional fracture surfaces of the 30BCZT composite was conducted to explain the observed highest tensile strength. From the SEM images shown in Figure 9, there was a significant difference between the 30BCZT composites and the other samples. Poor adhesion between the residual ZnO particles and the NR matrix was observed in the 0BCZT, whereas poor adhesion between the BCZT fillers and the NR matrix was observed in the 60BCZT, as indicated by the arrows in Figure 9 (a,c), respectively. In contrast, Figure 9(b) shows strong adhesion between the filler and the NR matrix in the 30BCZT composite.

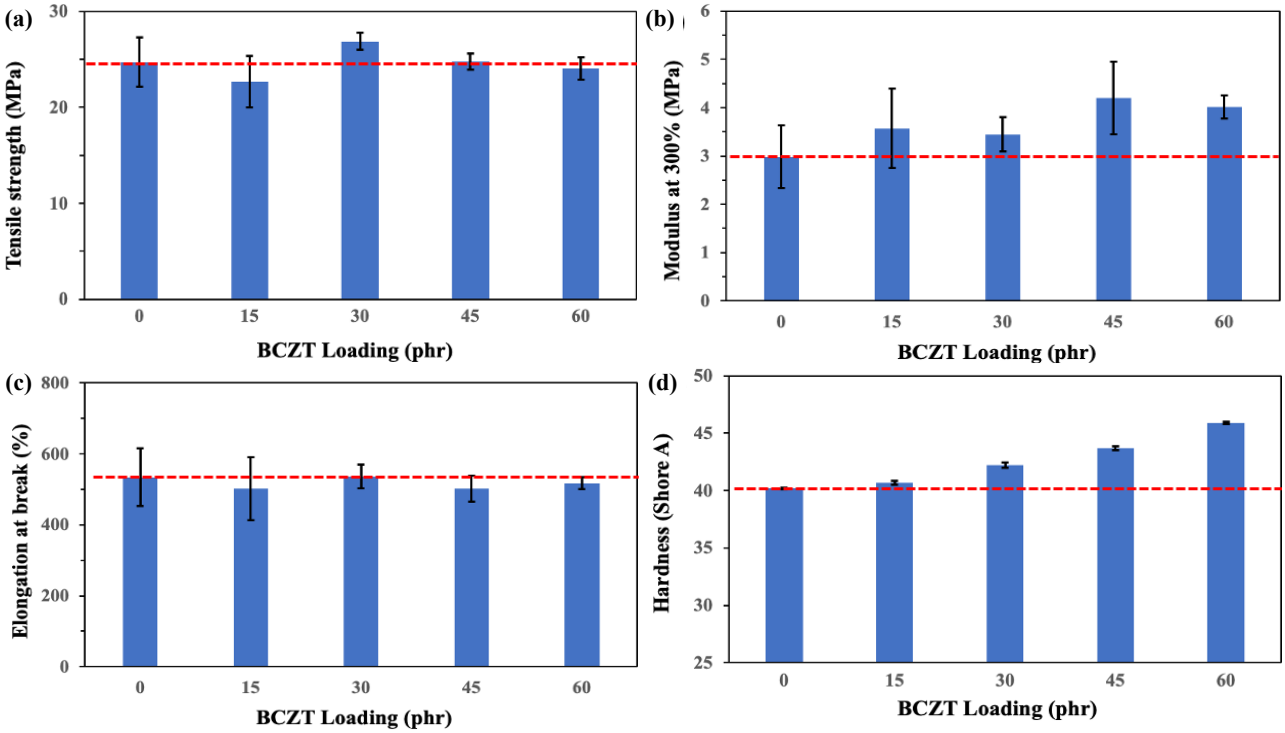


Figure 8. (a) tensile strength, (b) modulus at 300%, (c) elongation at break, and (d) hardness of the NR/BCZT composites as a function of BCZT loading.

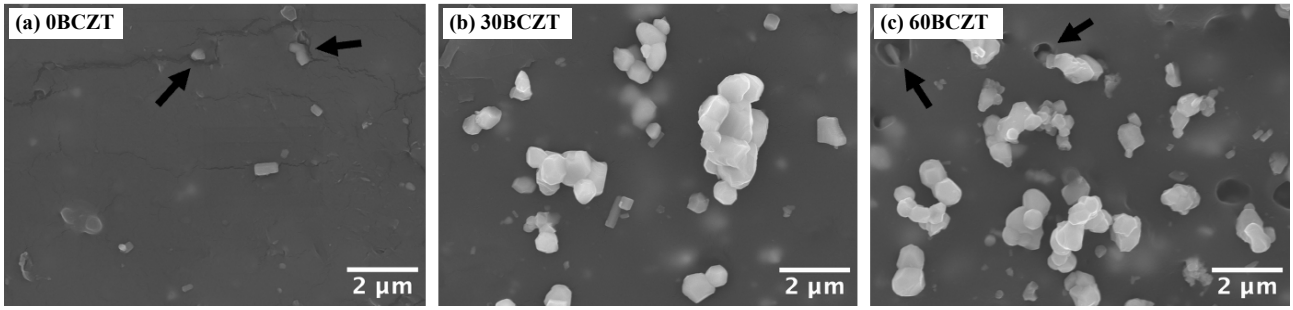


Figure 9. SEM images at high magnification of the NR/BCZT composites with BCZT loadings of (a) 0 phr, (b) 30 phr, and (c) 60 phr.

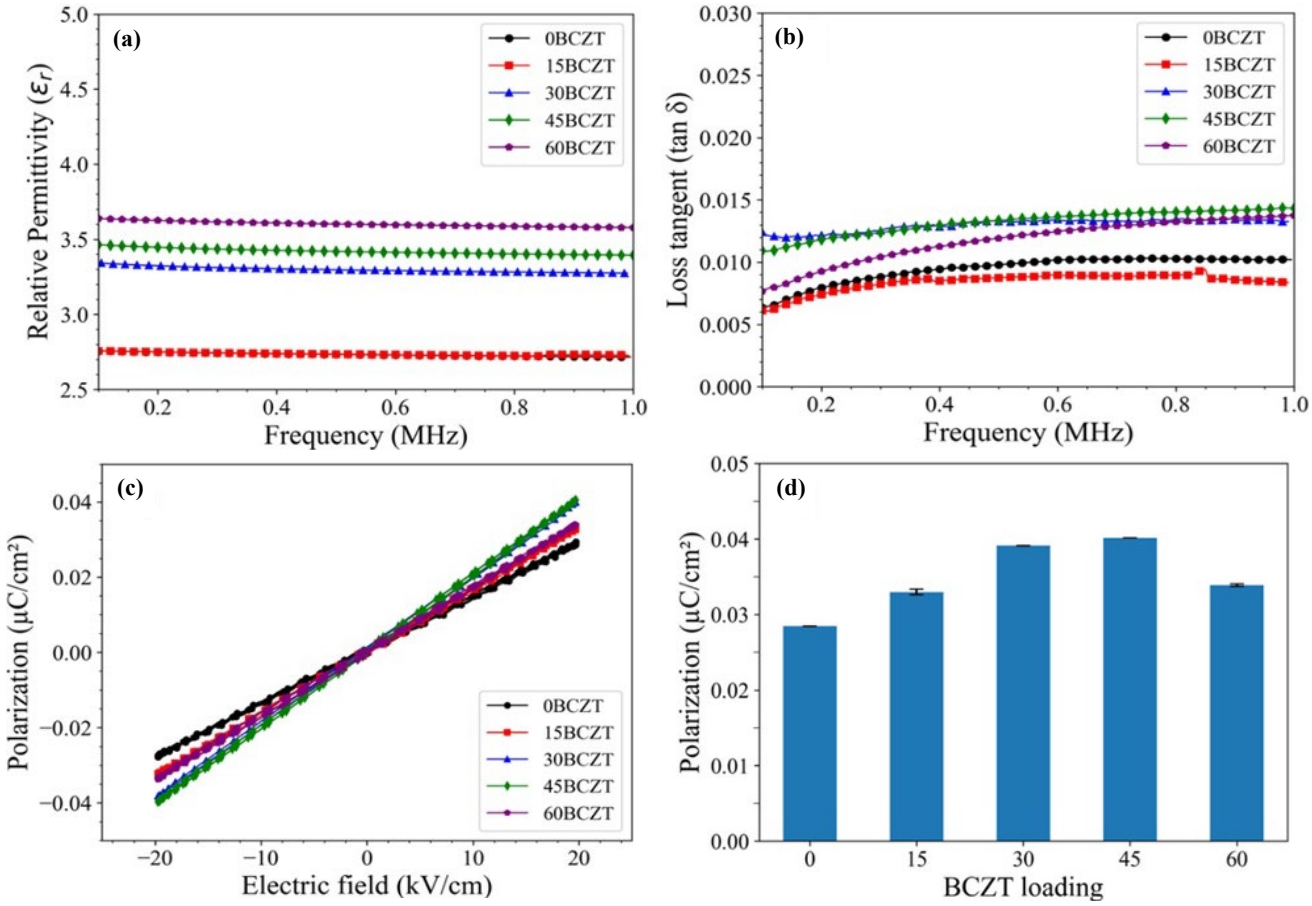


Figure 10. Frequency dependence of (a) dielectric permittivity, (b) loss tangent of the NR/BCZT composites. Comparison of, (c) field-induced polarization, and (d) average maximum polarization values of the NR/BCZT composites.

This optimal adhesion of BCZT filler at a loading of 30 phr enhanced the surface interaction between the BCZT filler and the NR matrix [9], accounting for the highest tensile strength. Also, when the BCZT filler content was further increased to 60 phr, cavities were observed in the 60BCZT composite which contributed to the decrease in tensile strength compared with the 30BCZT composite [11], as shown earlier in Figure 8(a).

3.5 Electrical properties of the NR/BCZT composites

Figure 10 compares the frequency-dependent dielectric properties and field-induced polarization of the NR/BCZT composites with increasing BCZT filler loading. It can be seen in Figure 10(a) that the addition of the BCZT filler improved the relative permittivity (ε_r) of the NR/BCZT composites over the frequency range from 0.1 MHz to 1 MHz. It was found that at a low BCZT loading of 15 phr, no increase in ε_r was observed at 0.1 MHz from 2.76 ± 0.07 (0 phr) to 2.76 ± 0.13 (15 phr). This result suggests that, the observed ε_r value at a low BCZT content is possibly attributed to induced polarization arising from the orientation of molecular dipoles and particle-molecule interfacial polarization, in combination with the spontaneous polarization of the BCZT ferroelectric filler [11]. Conversely, a noticeable enhancement in ε_r was observed when the BCZT filler content was further increased from 15 phr to 30 phr, with ε_r at 0.1 MHz increasing from 2.76 ± 0.13 to 3.34 ± 0.08, corresponding to an approximately 21.2% increase. However, a slight increase in ε_r at 0.1 MHz from 3.34 ± 0.08 to 3.64

± 0.07 (~8.9%) was observed when the BCZT content increased from 30 phr to 60 phr, respectively. A significant increase in ε_r for the NR/BCZT composites at high BCZT content (≥ 30 phr) may be attributed to the reduced interparticle distance with increasing BCZT loading, as described previously in section 3.3. This reduction in interparticle distance may enhance interfacial polarization arising from particle-particle interactions and further contribute to the increase in ε_r [10]. In contrast, no similar trend was observed in the frequency-dependent loss tangent (tan δ), which related to the dissipation of electromagnetic energy of the NR/BCZT composites with increasing BCZT content [11], as shown in Figure 10(b).

Further analysis of the field-induced polarization for the NR/BCZT composites at different BCZT loading content is shown in Figure 10 (c–d). Since the BCZT filler exhibits excellent ferroelectric properties, a ferroelectric hysteresis loop was initially expected to be observed in the NR/BCZT composites. However, this work found that the addition of BCZT filler up to 60 phr did not result in the presence of ferroelectric behavior in the NR/BCZT composites, as observed in Figure 10(c). Instead, linear field-dependent polarization was observed in all compositions, indicating that ferroelectric behavior was still not sufficiently pronounced in the NR/BCZT composites. Since no significant chemical interaction occurred between the NR matrix and the BCZT filler, as indicated by the FTIR spectra in Figure 3, this lack of interaction may also contribute to the absence of ferroelectric behavior in the NR/BCZT composites. These findings suggest that a higher BCZT loading (>60 phr) in combination with surface modification of the filler may be required to produce NR/BCZT composites exhibiting ferroelectric behavior. Although the NR/BCZT composites produced in this work did not exhibit the ferroelectric or nonlinear dielectric properties suitable for applications such as flexible wearable sensors and energy harvesters as reported in the literature discussed in section 1, they demonstrated linear dielectric behavior that may instead be suitable for energy-storage applications, such as dielectric capacitors [31]. Conversely, Figure 10(d) presents a comparison of the maximum polarization (P_{max}) induced at an applied electric field of 20 $kV \cdot cm^{-1}$ as a function of BCZT loading content. A slight increase in P_{max} was observed with increasing BCZT content, from 0.02845 ± 0.00002 $\mu C \cdot cm^{-2}$ (0 phr) to 0.04013 ± 0.00001 $\mu C \cdot cm^{-2}$ (45 phr). However, when BCZT loading was further increased to 60 phr, the observed P_{max} slightly decreased to 0.03388 ± 0.00017 $\mu C \cdot cm^{-2}$. This reduction in the observed P_{max} at 60 phr composition may be attributed to the presence of porosity that could hinder the orientation of polarization under the applied electric field [4].

4. Conclusions

In this work, lead-free piezoceramic-filled natural rubber composites were developed by incorporating BCZT lead-free piezoceramic fillers into a NR matrix with filler loading ranging from 0 phr to 60 phr. The curing characteristic result showed that as the BCZT filler content increased, the vulcanization reaction rate was enhanced, leading to a decrease in the cure time of the NR/BCZT composites. Moreover, this work found that the addition of BCZT filler into NR reduced the tensile strength of the NR/BCZT composites, except for the 30BCZT composites, which exhibited strong adhesion between the BCZT filler and the NR matrix as observed in high-magnification SEM images. In contrast, the hardness of the NR/BCZT composites slightly increased with increasing BCZT filler content. Interestingly, no improvement in dielectric permittivity was observed at a low BCZT loading of 15 phr, whereas a noticeable enhancement occurred when the BCZT filler content was further increased to 30 phr. The 3D visualizations obtained by SR-XTM, combined with the quantitative analysis of SEM images, showed that increasing the BCZT content primarily increased the population density of BCZT particle regions while reducing their interparticle spacing. This reduction in interparticle spacing may enhance interfacial polarization in the NR/BCZT composites and play a significant role in their observed electrical properties. This study demonstrates that combining SR-XTM with other materials characterization techniques provides valuable insights into structure-property relationships and contributes to a better understanding of the development of lead-free piezoceramic-filled natural rubber composites.

Acknowledgments

This study was supported by the Thammasat University Research Fund under Contract number TUFT113/2567. In addition, the authors thank the Synchrotron Light Research Institute, Thailand, for access to beamline BL1.2W: X-ray tomography microscopy.

References

[1] J. Rödel and J.-F. Li, "Lead-free piezoceramics: Status and perspectives," *MRS Bulletin*, vol. 43, no. 8, pp. 576–580, 2018

[2] M. Smith, and S. Kar-Narayan, "Piezoelectric polymers: theory, challenges and opportunities," *International Materials Reviews*, vol. 67, no. 1, pp. 65–88, 2022

[3] X. Li, G. Wu, C. Gao, R. Bao, and C. Pan, "Flexible electronic devices and wearable sensors based on liquid metals," *MetalMat*, vol. 2, no. 1, p. e70000, 2025.

[4] H. Hosseinzadeh, H. Oveisi, and K. Yazdani, "Review: Enhancing dielectric polymer performance via inorganic fillers," *Journal of Materials Science*, vol. 60, no. 42, pp. 20160–20190, 2025.

[5] L. Muhamad, M. A. Saparin, and H. Salleh, "Performance of a piezoelectric energy harvester with rubber compound modificatio," *Journal of Physics: Conference Series*, vol. 2721, p. 012002, 2024.

[6] J. E. Q. Quinsaat, T. de Wild, F. A. Nüesch, D. Damjanovic, R. Krämer, G. Schürch, D. Häfliger, F. Clemens, T. Sebastian, M. Dascalu, and D. M. Opris, "Stretchable piezoelectric elastic composites for sensors and energy generators," *Composites Part B: Engineering*, vol. 198, p. 108211, 2020.

[7] J. Zhang, J. Wang, C. Zhong, Y. Zhang, Y. Qiu, and L. Qin, "Flexible electronics: Advancements and applications of flexible piezoelectric composites in modern sensing technologies," *Micromachines*, vol. 15, no. 8, p. 982, 2024.

[8] M. Mureddu, A. Reyes-Montero, S. Lopez-Esteban, J. F. Bartolome, S. Enzo, L. Pardo, and S. Garroni, "Hallmarks of BCZT-based piezoceramics: From chemical fundamental to processing route and biomedical applications," *Boletín de la Sociedad Española de Cerámica y Vidrio*, vol. 64, no. 3, p. 100434, 2025.

[9] S. Salaeh, N. Muensit, P. Bomlai, and C. Nakason, "Ceramic/natural rubber composites: Influence types of rubber and ceramic

materials on curing, mechanical, morphological, and dielectric properties," *Journal of Materials Science*, vol. 46, no. 6, pp. 1723–1731, 2010.

[10] N. González, M. d. À. Custal, G. N. Tomara, G. C. Psarras, J.-R. Riba, and E. Armelin, "Dielectric response of vulcanized natural rubber containing $BaTiO_3$ filler: The role of particle functionalization," *European Polymer Journal*, vol. 97, pp. 57–67, 2017.

[11] A. A. El-Gamal, "Electrical and mechanical characterization of vulcanized natural rubber filled with $BaTiO_3$ ceramic filler," *Journal of Thermoplastic Composite Materials*, vol. 34, no. 3, pp. 287–302, 2019.

[12] L. Chen, W. Zhou, J. Lu, J. Li, W. Zhang, N. Huang, L.Wu, and L. Li, "Unveiling reinforcement and toughening mechanism of filler network in natural rubber with synchrotron radiation X-ray nano-computed tomography," *Macromolecules*, vol. 48, no. 21, pp. 7923–7928, 2015.

[13] M. Matsubara, S. Teramoto, T. Komatsu, S. Furuta, M. Kobayashi, S. Kawamura, A. Nagatani, N. Tsujiuchi, and A. Ito, "Three-dimensional strain evaluation of short-fiber-reinforced natural rubber using micro X-ray computed tomography," *Polymer Testing*, vol. 111, Art. no. 107625, 2022.

[14] R. Mashita, Y. Bito, K. Uesugi, M. Hoshino, I. Kageyuki, H. Kishimoto, W. Yashiro, and T. Kanaya, "Insights into the cavitation morphology of rubber reinforced with a nano-filler," *Scientific Reports*, vol. 13, no. 1, Art. no. 5805, 2023.

[15] A. P. Parra, M. Vlasova, and P. A. M. Aguilar, "Adsorptive properties of $MgCO_3$–$CaCO_3$ Sargasso treated in air and deficient of oxygen," *MRS Advances*, vol. 9, no. 3, pp. 148–154, 2024.

[16] M. Mureddu, J. F. Bartolomé, S. Lopez-Esteban, M. Dore, S. Enzo, Á. García, S. Garroni, and L. Pardo, "Solid state processing of BCZT piezoceramics using ultra low synthesis and sintering temperatures," *Materials*, vol. 16, no. 3, p. 945, 2023.

[17] S. Sahoo, U. Dash, S. K. S. Parashar, and S. M. Ali, "Frequency and temperature dependent electrical characteristics of $CaTiO_3$ nano-ceramic prepared by high-energy ball milling," *Journal of Advanced Ceramics*, vol. 2, no. 3, pp. 291–300, 2013.

[18] X. W. Wang, B. H. Zhang, Y. Y. Li, Y. C. Shi, L. Y. Sun, G. Feng, C. L. Li, Y. F. Liang, Y. P. Zheng, S. Y. Shang, J. Shang, Y. C. Hu, and S. Q. Yin, "Structure, dielectric, and ferroelectric properties of $Ba_{0.85}Ca_{0.15}Zr_{0.1}Ti_{0.9}O_3$ ceramics sintered at various temperatures," *Journal of Materials Science: Materials in Electronics*, vol. 31, no. 6, pp. 4732–4742, 2020.

[19] J. Intapun, T. Rungruang, S. Suchat, B. Cherdchim, and S. Hiziroglu, "The Characteristics of natural rubber composites with klason lignin as a green reinforcing filler: Thermal stability, mechanical and dynamical properties," *Polymers*, vol. 13, no. 7, p. 1109, 2021.

[20] T. T. M. Phan, N. C. Chu, V. B. Luu, H. N. Xuan, D. T. Pham, I. Martin, and P. Carrière, "Enhancement of polarization property of silane-modified $BaTiO_3$ nanoparticles and its effect in increasing dielectric property of epoxy/$BaTiO_3$ nano-composites," *Journal of Science: Advanced Materials and Devices*, vol. 1, no. 1, pp. 90–97, 2016.

[21] M. Przybyszewska, and M. Zaborski, "The effect of zinc oxide nanoparticle morphology on activity in crosslinking of carboxylated nitrile elastomer," *Express Polymer Letters*, vol. 3, no. 9, pp. 542–552, 2009.

[22] E. Bayraktar, S. D. Antolovich, and C. Bathias, "New developments in non-destructive controls of the composite materials and applications in manufacturing engineering," *Journal of Materials Processing Technology*, vol. 206, no. 1–3, pp. 30–44, 2008.

[23] S. Konruang, A. Srisook, P. Buaphet, F. Tayeh, and W. Naebpetch, "Preparation of lead-free X-ray shielding materials based on natural rubber/barium sulfate composites," *ASEAN Journal of Scientific and Technological Reports*, vol. 25, no. 2, pp. 59–66, 2022.

[24] A. Lanna, M. Suklueng, C. Kasagepongsan, and S. Suchat, "Performance of novel engineered materials from epoxy resin with modified epoxidized natural rubber and nanocellulose or nanosilica," *Advances in Polymer Technology*, vol. 2020, no. 1, p. 2123836, 2020.

[25] L. Caggiu, C. Cau, M.Mureddu, S. Enzo, F. Murgia, L. Pardo, S. Lopez-Esteban, J. F. Bartolomé, G. Mulas, R. Orrù, and S. Garroni, "High purity, crystallinity and electromechanical sensitivity of lead-free $(Ba_{0.85}Ca_{0.15})(Zr_{0.10}Ti_{0.90})O_3$ synthesized using an EDTA/glycerol modified pechini method," *Materials*, vol. 18, no. 5, p. 1180, 2025.

[26] M. Mazaheri, A. M. Zahedi, and S. K. Sadrnezhaad, "Two-step sintering of nanocrystalline ZnO compacts: Effect of temperature on densification and grain growth," *Journal of the American Ceramic Society*, vol. 91, no. 1, pp. 56–63, 2008.

[27] M. Stampanoni, R. Mokso, F. Marone, J. Vila-Comamala, S. Gorelick, P. Trtik, K. Jefimovs, and C. David, "Phase-contrast tomography at the nanoscale using hard x rays," *Physical Review B*, vol. 81, no. 14, p. 140105, 2010.

[28] C. A. Schneider, W. S. Rasband, K. W. Eliceiri, "NIH image to ImageJ: 25 years of image analysis," *Nature Methods*, vol. 9, pp. 671–675, 2012.

[29] ISO 13322-1:2014. Particle size analysis - Image analysis methods - Part 1: Static image analysis methods, 2014.

[30] ISO 9276-2. Representation of results of particle size analysis - Part 2: Calculation of average particle sizes/diameters and moments from particle size distributions, 2014.

[31] L. Dou, Y.-H. Lin, and C.-W. Nan, "An overview of linear dielectric polymers and their nanocomposites for energy storage," Molecules, vol. 26, no. 20, p. 6148, 2021.